



Tuning the atomic configuration of Co-N-C electrocatalyst enables highly-selective H₂O₂ production in acidic media

Wei Liu^a, Chang Zhang^a, Jingjing Zhang^a, Xiao Huang^a, Min Song^a, Jingwen Li^a, Feng He^a, Haiping Yang^b, Jian Zhang^{a,*}, Deli Wang^{a,*}

^a Key Laboratory of Material Chemistry for Energy Conversion and Storage, Ministry of Education, Hubei Key Laboratory of Material Chemistry and Service Failure, School of Chemistry and Chemical Engineering, Huazhong University of Science and Technology, Wuhan 430074, PR China

^b State Key Laboratory of Coal Combustion, Huazhong University of Science and Technology, Wuhan 430074, PR China

ARTICLE INFO

Keywords:

Oxygen reduction reaction
Two-electron selectivity
Electrocatalyst
Cobalt single-atoms
H₂O₂ electrosynthesis

ABSTRACT

The oxygen reduction reaction (ORR) is essential for both energy conversion devices and green hydrogen peroxide (H₂O₂) synthesis. Whereas, it remains a challenge to efficiently tune the oxygen reduction selectivity toward the target applications. Herein, we designed two kinds of Co-N-C materials with encapsulated Co nanoparticles (Co_{NP}-N-C) and with atomically dispersed cobalt atoms strongly embedded into nitrogen-doped carbon nanotubes (Co_{SA}-N-CNTs), and successfully realized the ORR pathway transformation from four-electron (4e⁻) to two-electron (2e⁻) for high-performance H₂O₂ production. This tunability is ascribed to the modification of the atomic configuration of the Co-N-C catalyst. Remarkably, when employing Co_{SA}-N-CNTs material as a 2e⁻ ORR catalyst, the assembled electrode exhibits a high H₂O₂ production rate of approximately 974 ± 25 mmol g_{cat}⁻¹ h⁻¹, along with an ultra-fast organic matter degradation performance. This work provides an efficient strategy for tuning oxygen reduction selectivity via a simple structure tuning of the materials for specific applications.

1. Introduction

The oxygen reduction reaction (ORR) usually takes two pathways, in which the four-electron (4e⁻) reaction is to produce water, the two-electron (2e⁻) reaction is to generate H₂O₂ product. The former is usually applied to energy conversion systems. The latter can ensure environmentally friendly H₂O₂ synthesis [1,2]. In the last few decades, tremendous achievements have been made in the development of 4e⁻ ORR catalysts for fuel cells and metal-air batteries. In particular, according to the rapid development and urgent demand of green synthesis, exploring the high-performance 2e⁻ ORR catalyst toward H₂O₂ synthesis has recently been a hot research area. H₂O₂ is widely used in various fields such as medical disinfection, paper bleaching, wastewater treatment, and fine chemical synthesis due to its “green” and strong oxidation property [3,4]. The 2e⁻ ORR has recently attracted widespread research interest since it is a green, energy-saving, and economic H₂O₂ production technology. Moreover, the generated H₂O₂ products can be used on-site, so it is considered the most promising alternative approach to replace the traditional anthraquinone process [5,6].

However, the core reaction of O₂ reduction suffers from low kinetics with high overpotential and also presents a competitive relationship between the 4e⁻ and 2e⁻ reaction pathways, which will affect the efficiency of product generation [7–9]. Therefore, the rational design and fabrication of ORR electrocatalysts with high activity and stability while achieving high 2e⁻ selectivity are essential for H₂O₂ electrosynthesis.

To date, the most advanced electrocatalysts for electrochemical synthesis of H₂O₂ in acidic conditions are limited to noble metal-based electrocatalysts (Pt-Hg, Pd-Hg, Au-Pd, etc) [10–12], in terms of their excellent 2e⁻ selectivity and stability in acidic electrolytes. But they suffer from the high cost and scarce resources, which cannot be large-scale application in practice. Fortunately, the earth-abundant transition metal cobalt and nitrogen coordinated carbonaceous materials (labeled as Co-N-C) have recently emerged, and shown great potential for electrocatalytic ORR to H₂O₂ production in acidic electrolytes [13,14]. Currently, the most efficient method for the preparation of Co-N-C materials is pyrolysis of metal-organic frameworks (MOFs), which can maintain excellent porous structure with abundant heteroatomic dopants and active metal centers, leading to high

* Corresponding authors.

E-mail addresses: zhangjian7@hust.edu.cn (J. Zhang), wangdl81125@hust.edu.cn (D. Wang).

<https://doi.org/10.1016/j.apcatb.2022.121312>

Received 14 December 2021; Received in revised form 26 January 2022; Accepted 10 March 2022

Available online 12 March 2022

0926-3373/© 2022 Elsevier B.V. All rights reserved.

electrochemical performance [15,16]. However, the inevitable cobalt nanoparticles formation during the pyrolysis would dramatically reduce the current efficiency of H_2O_2 electrosynthesis, since it dominates the competitive reaction of 4e^- ORR [17,18]. In addition, the obtained materials normally present powder or granular morphology, which results in the high mass, ions, and electrons transfer resistance during the electrocatalysis. Inversely, avoiding the cobalt nanoparticles formation and simultaneously establishing a tightly connected network for the H_2O_2 electrosynthesis is highly expected.

Herein, we report that the ORR selectivity of Co-N-C catalyst can be effectively transformed from 4e^- to 2e^- pathway by tuning the structure properties. The constructed $\text{Co}_{\text{NP}}\text{-N-C}$ catalyst with plentiful cobalt nanoparticles encapsulated in carbon matrix shows distinct 4e^- ORR performance. The fabricated $\text{Co}_{\text{SA}}\text{-N-CNTs}$ that are dominated by atomically dispersed cobalt atoms strongly embedded into nitrogen-doped carbon nanotubes exhibit high 2e^- selectivity and stability for acidic H_2O_2 production. Impressively, the $\text{Co}_{\text{SA}}\text{-N-CNTs}$ catalysts as the cathode catalyst applied to the flow cell device reveal a high H_2O_2 production rate and enable efficient degradation of kinds of organic pollutants. The extremely excellent 2e^- ORR performance is attributed to the integrated merits of the atomically dispersed active Co- N_x species and the three-dimensional conductive network of the carbon nanotubes.

2. Experimental section

2.1. Synthesis of ZIF-67 precursors

In a typical synthesis, 1.455 g of $\text{Co}(\text{NO}_3)_2 \cdot 6\text{H}_2\text{O}$ and 1.642 g of 2-methylimidazole (2-MeIm) were dissolved in 40 mL methanol solution, respectively. Then, the dispersed 2-MeIm solution was quickly poured into the $\text{Co}(\text{NO}_3)_2 \cdot 6\text{H}_2\text{O}$ solution under vigorous stirring for 10 s, and then the mixed solution was aged for 24 h at room temperature. Finally, the purple precipitate was collected by centrifugation, washed with methanol and ethanol, and then dried in a vacuum oven at 60°C to obtain ZIF-67 precursor powder.

2.2. Synthesis of $\text{Co}_{\text{SA}}\text{-N-CNTs}$ and $\text{Co}_{\text{NP}}\text{-N-C}$

The ZIF-67 precursor was maintained at 900°C for 3 h (heating rate of 2°C min^{-1}) under Ar/H_2 (10 vol%) atmosphere with a flow rate of 100 sc.c.m. Afterward, the acid-leaching approach was employed to heat at 60°C for 8 h in 0.5 M H_2SO_4 solution to remove the inactive Co species in the polyhedral framework. The samples were collected by suction filtration and washed to $\text{pH} = 7$, and dried overnight under vacuum conditions to obtain the black powder, which was defined as

$\text{Co}_{\text{SA}}\text{-N-CNTs}$. Similarly, except for changing the reaction condition to Ar atmosphere, the other conditions remain the same, and the resulting product is defined as $\text{Co}_{\text{NP}}\text{-N-C}$. For comparison, ZIF-67 powder was annealed at $700\text{--}1000^\circ\text{C}$ in two different atmospheres. The products prepared in Ar/H_2 atmosphere were defined as Co-N-CNTs-X ($X = 700\text{--}1000^\circ\text{C}$), and the products prepared in Ar atmosphere were defined as $\text{Co}_{\text{NP}}\text{-N-C-X}$.

3. Result and discussion

3.1. Synthesis and characterizations of catalysts

The fabrication of $\text{Co}_{\text{NP}}\text{-N-C}$ and $\text{Co}_{\text{SA}}\text{-N-CNTs}$ is illustrated in Fig. 1. First, the ZIF-67 purple powder with zeolite structure (Fig. S1) was synthesized using cobalt nitrate and 2-methylimidazole by a conventional method [19]. Subsequently, the powder was directly pyrolyzed at 900°C for 3 h in an argon (Ar) atmosphere and then underwent the acid-leaching [20,21], the product with abundant Co nanoparticles encapsulated in the nitrogen-doped carbon matrix ($\text{Co}_{\text{NP}}\text{-N-C}$) was obtained. Interestingly, by changing the pyrolysis atmosphere into the Ar/H_2 with the same procedures, the interconnected nitrogen-doped carbon nanotube structures with atomically dispersed Co- N_x species ($\text{Co}_{\text{SA}}\text{-N-CNTs}$, see below) were obtained, as detailed shown in Supporting Information.

Fig. 2a shows the scanning electronic microscopy (SEM) images of $\text{Co}_{\text{NP}}\text{-N-C}$, which maintains the initial polyhedral morphology of pure ZIF-67 (Fig. S1) but becomes very rough with many irregular particles distributed. Transmission electron microscopy (TEM) image of Fig. 2b and S2 shows that $\text{Co}_{\text{NP}}\text{-N-C}$ contains plenty of Co NPs with diameters of ~ 30 nm, as evidenced by the corresponded (111) crystal plane of metallic cobalt (Fig. 2c), which can be ascribed to the protection of carbon frameworks during the acid-leaching process. Fig. 2d shows the SEM images of $\text{Co}_{\text{SA}}\text{-N-CNTs}$ are composed of numbers of tiny carbon nanotubes, which are interconnected by extension and growth based on the initial framework structure. The corresponding TEM image (Fig. 2e) also confirms that these CNTs grow uniformly on the framework surface with a thickness of ~ 10 nm. The multi-layer graphitic carbon lattice fringes (0.355 nm) at the edges of the carbon nanotubes can be observed in Fig. 2f, and no metallic phase cobalt lattice fringes are observed. High-angle annular dark-field scanning transmission electron microscopy (HAADF-STEM) and the corresponding energy-dispersive X-ray energy dispersive spectroscopy (EDS) mapping images (Fig. 2g) reveal that C, N, and Co elements are homogeneously distributed over the $\text{Co}_{\text{SA}}\text{-N-CNTs}$, and the atomic ratio of Co element is about 0.11 at%. Further, the Co content of the $\text{Co}_{\text{SA}}\text{-N-CNTs}$ catalyst was also determined by inductively

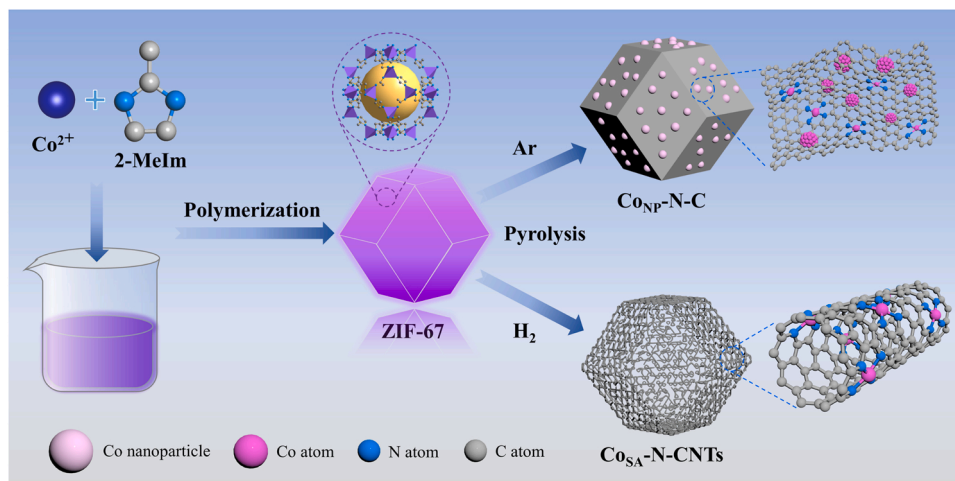


Fig. 1. Schematic illustration for the preparation of $\text{Co}_{\text{SA}}\text{-N-CNTs}$ and $\text{Co}_{\text{NP}}\text{-N-C}$ catalysts.

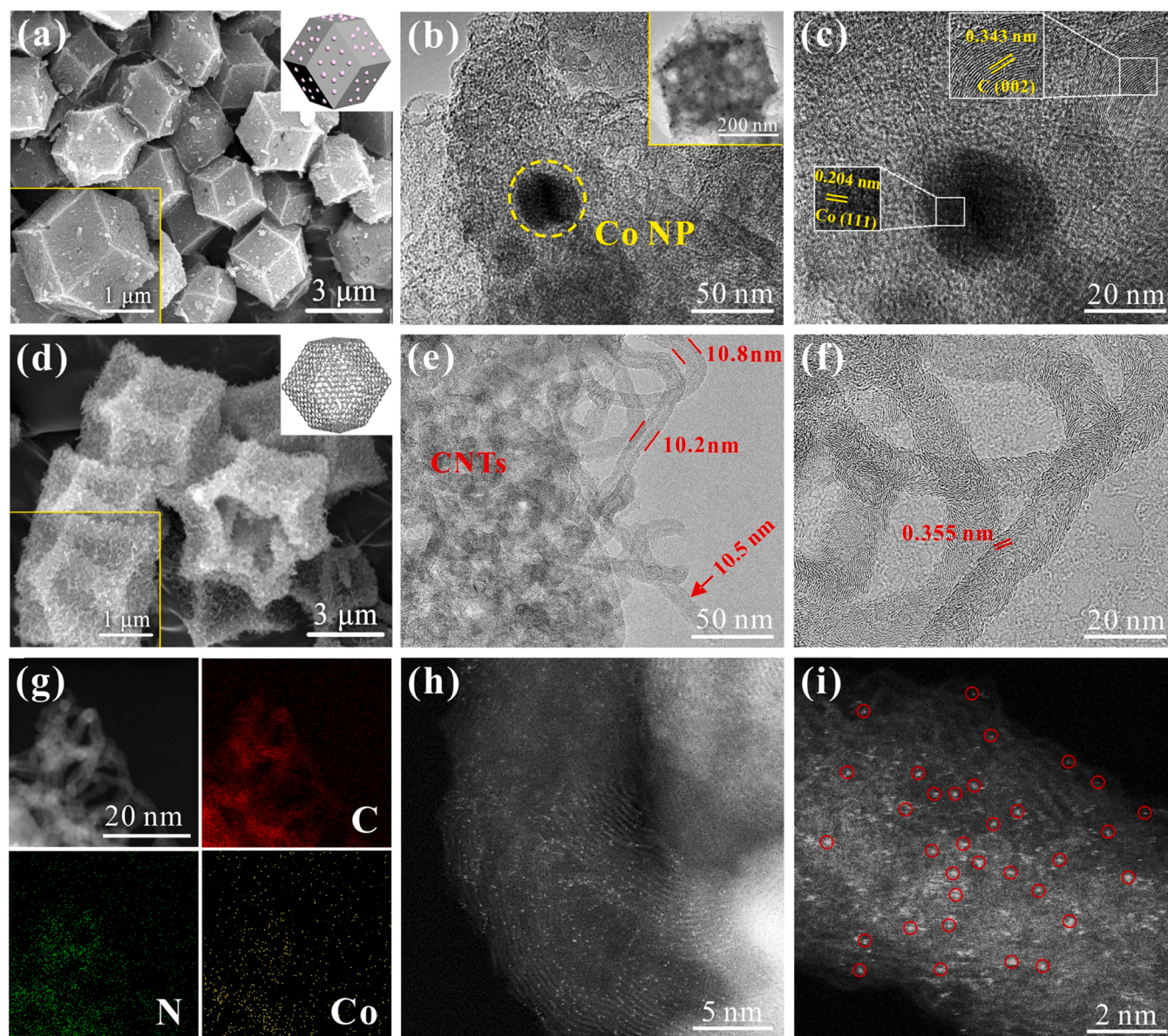


Fig. 2. (a) SEM images and (b, c) TEM images of $\text{Co}_{\text{NP}}\text{-N-C}$. (d) SEM images and (e, f) TEM images of $\text{Co}_{\text{SA}}\text{-N-CNTs}$. (g) HAADF-STEM and corresponding EDS mapping images of C, N, and Co elements. (h) and (i) Magnified AC HAADF-STEM images of the $\text{Co}_{\text{SA}}\text{-N-CNTs}$.

coupled plasma-mass spectrometry (ICP-MS), which is 0.79 wt% (Table S1). The aberration-corrected (AC) HAADF-STEM images (Figs. 2h and i) show that many discrete white bright spots are embedded into the edge area and the interlayer of CNTs in the $\text{Co}_{\text{SA}}\text{-N-CNTs}$, indicating that individual Co atoms are homogeneously dispersed throughout the carbon frameworks. Further, the specific surface area and pore-size distribution were analyzed by nitrogen absorption-desorption isotherms measurements as shown in Fig. S3. As expected, the $\text{Co}_{\text{SA}}\text{-N-CNTs}$ sample exhibits a larger Brunauer-Emmett-Teller (BET) specific surface area ($409 \text{ m}^2 \text{ g}^{-1}$) than $\text{Co}_{\text{NP}}\text{-N-C}$ ($303 \text{ m}^2 \text{ g}^{-1}$) due to the numerous CNTs, and its pore size is predominantly micropores and mesoporous ($< 7 \text{ nm}$). The three-dimensional carbon nanotube network structure in $\text{Co}_{\text{SA}}\text{-N-CNTs}$ can provide more active sites and promote electron transfer during the reaction, which may be more favorable for H_2O_2 generation.

X-ray diffraction (XRD) patterns of Fig. 3a reveal that the diffraction peaks at 26° and 43° correspond to the (002) and (100) crystal planes of graphitic carbon. The $\text{Co}_{\text{NP}}\text{-N-C}$ sample contains two metallic Co diffraction peaks at 44.2° and 51.5° , whereas $\text{Co}_{\text{SA}}\text{-N-CNTs}$ did not show

any features of metallic Co (Fig. S4). From Raman spectra of Fig. 3b, the peaks near 1350 and 1600 cm^{-1} represent defective carbon (D band) and graphitized carbon (G band), respectively. The intensity ratio of the D band and G band ($I_{\text{D}}/I_{\text{G}}$) can be used to clarify the graphitization degree of carbon [22]. The $I_{\text{D}}/I_{\text{G}}$ value of $\text{Co}_{\text{SA}}\text{-N-CNTs}$ (0.93) is smaller than $\text{Co}_{\text{NP}}\text{-N-C}$ (0.99), manifesting that $\text{Co}_{\text{SA}}\text{-N-CNTs}$ have a higher degree of graphitization than $\text{Co}_{\text{NP}}\text{-N-C}$ due to the presence of individual carbon nanotubes [23]. The chemical elements and composition of the prepared samples were analyzed by X-ray photoelectron spectroscopy (XPS). The high-resolution Co 2p spectra (Fig. 3c) of $\text{Co}_{\text{SA}}\text{-N-CNTs}$ are mainly assigned to Co^{2+} (779.2 and 794.6 eV), Co- N_x (780.7 and 796.1 eV), and satellite peaks [24–26], and the presence of metallic cobalt is not identified, signifying that the Co configuration in $\text{Co}_{\text{SA}}\text{-N-CNTs}$ is more likely to the single-atom characteristic with $\text{Co}^{2+}\text{-N}$ coordination state [27]. However, the Co 2p spectra of $\text{Co}_{\text{NP}}\text{-N-C}$ can be divided into four pairs of fitting peaks, corresponding to Co^0 (778.5 and 793.7 eV), Co- N_x (780.6 and 796 eV), Co^{3+} (782 and 797.4 eV), and satellite peaks, respectively [28–30]. Among them, Co^{3+} species are caused by the oxidation of Co nanoparticles, which is

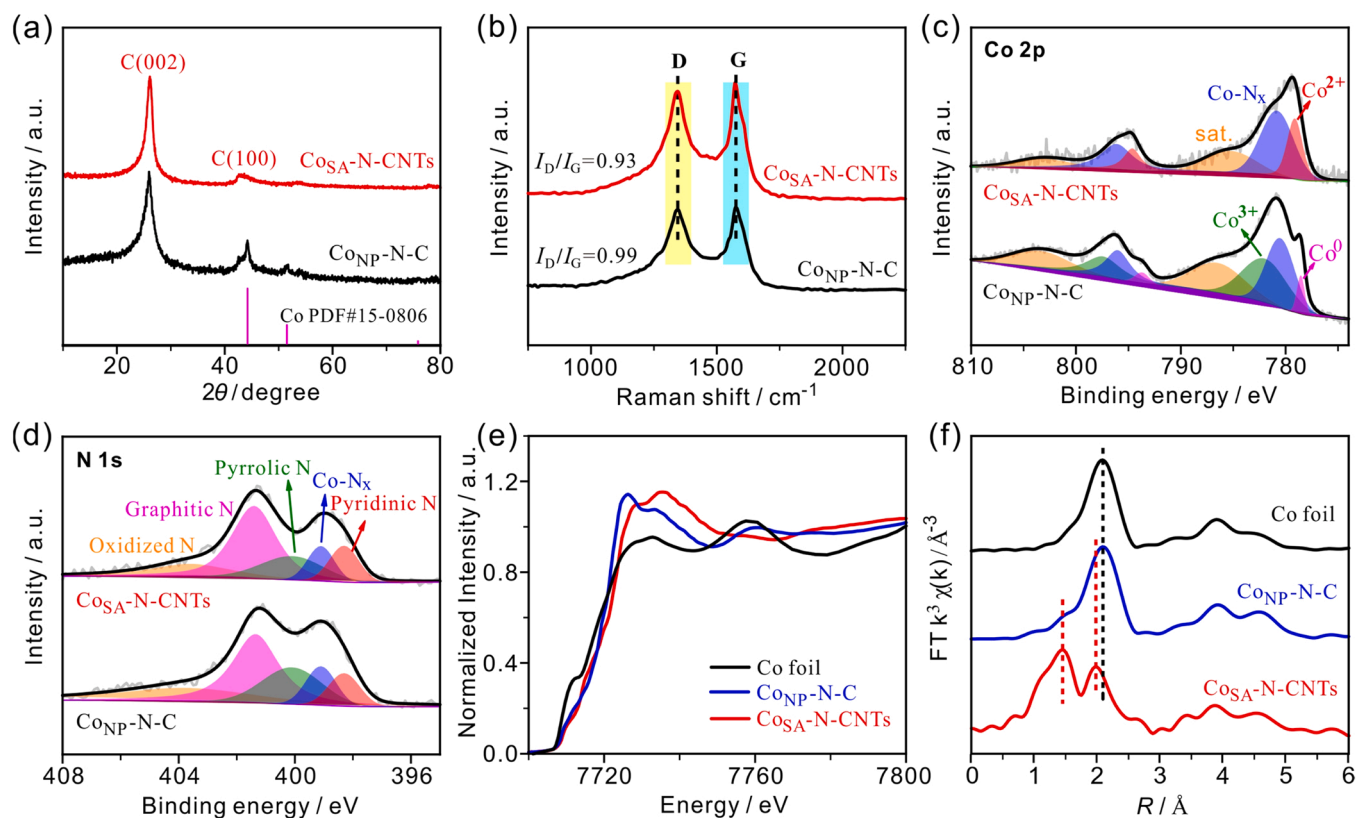


Fig. 3. (a) XRD patterns, (b) Raman spectra, (c) and (d) The high-resolution Co 2p and N 1s XPS spectra of CoSA-N-CNTs and CoNP-N-C, respectively. (e) Co K-edge XANES spectra and (f) FT-EXAFS spectra at Co K-edge of CoSA-N-CNTs, CoNP-N-C, and Co foil.

consistent with the results (Fig. S9c) of the composite structure of carbon nanotubes and Co nanoparticles. From the high-resolution N 1s spectra in Fig. 3d, they can be deconvoluted into five peaks located at 398.3, 399.1, 400.1, 401.35, and 403.5 eV, corresponding to the pyridinic-N, Co-N_x, pyrrolic-N, graphitic-N, and oxidized N, respectively [31,32]. The results show that CoSA-N-CNTs have a higher graphitic-N content than CoNP-N-C, suggesting that Co-N_x species are embedded into CNTs.

The chemical states and local coordination environment of Co atoms were further revealed by X-ray absorption near-edge structure (XANES) and extended X-ray absorption fine structure (EXAFS) spectra. Fig. 3e and f show the absorption edge positions and the corresponding Fourier transform (FT) EXAFS spectra of CoSA-N-CNTs, CoNP-N-C, and Co foil, respectively. The main sharp peak at 2.14 Å in CoNP-N-C is attributed to the Co-Co paths of Co metal. In contrast, the peak at 1.45 Å in CoSA-N-CNTs is attributed to the most typical Co-N coordination bonds. The structural parameters by EXAFS fitting analysis revealed that the quantitative coordination number of Co atom is 3.9, implying the Co-N₄ coordination structure of CoSA-N-CNTs catalyst (Table S2). Notably, a small accompanying peak is located at 1.96 Å, which partially overlaps with the Co-Co peak. As reported by Fei's group, the CoN₄C₄ moiety in carbonaceous matrix with a similar bimodal configuration, attributed to backscattering between metal atoms and light atoms (i.e., C, N, and O atoms) instead of metal aggregates [33,34]. In general, the above results indicate that the Co configuration in CoSA-N-CNTs catalysts is dominated by single atoms, whereas CoNP-N-C samples mainly contain Co nanoparticles.

3.2. Electrocatalytic ORR performance of catalysts

The ORR electrochemical performance of all catalysts was evaluated using the rotating ring-disk electrode (RRDE) measurements in the O₂-saturated 0.5 M H₂SO₄ electrolyte. All potentials were calibrated to reversible hydrogen electrodes (vs. RHE), the rotation speed was

maintained at 1600 rpm during the test, and the platinum ring potential was held at 1.2 V (vs. RHE) to quantify the H₂O₂ generated on the disk electrode. Fig. 4a shows the linear sweep voltammetry (LSV) curves of CoSA-N-CNTs and CoNP-N-C catalysts. According to disk and ring electrode current densities, CoSA-N-CNTs catalyst shows lower onset potential (0.7 V) and diffusion-limiting disk current density (−2.9 mA cm^{−2} at 0.1 V) in comparison with the CoNP-N-C catalyst (−3.4 mA cm^{−2} at 0.1 V), but it exhibits a much higher ring electrode current density in a long potential range from 0.1 V to 0.6 V than CoNP-N-C catalyst, implying that CoSA-N-CNTs catalyst with atomically dispersed Co active sites has higher 2e[−] selectivity for ORR than the counterpart of CoNP-N-C catalyst. As shown from the calculated results of H₂O₂ selectivity (H₂O₂/%) and the electron transfer number (n) value in Fig. 4b, the CoSA-N-CNTs shows extremely high H₂O₂ selectivity (more than 95% in a long potential range of 0.35–0.7 V), and the corresponding n value is infinitely close to 2, which is much superior to CoNP-N-C (H₂O₂/% < 30% and n > 3.5) for H₂O₂ electrosynthesis (Fig. 3g).

Furthermore, CoSA-N-CNTs catalyst shows a good ability to inhibit the H₂O₂ reduction reaction (H₂O₂RR). As shown in Fig. 4c, the polarization curve of CoSA-N-CNTs (red dashed line) has negligible current density compared with CoNP-N-C (black dashed line), suggesting the inactivity of H₂O₂RR, which can prove its inherent high selectivity of 2e[−] ORR. Moreover, the active center of the catalyst is investigated through the thiocyanate ions (SCN[−]) poisoning experiment. The SCN[−] can strongly bind to the locally coordinated single metal atomic sites, so it selectively prevents the adsorption of reaction intermediates to the central metal active site [35]. The polarization curves of CoSA-N-CNTs (Fig. S5) show that the SCN[−] will poison the coordinated Co atoms, resulting in a significant decrease in terms of the onset potential and disk current, meaning that the Co single atoms serve as the active center for ORR.

Notably, CoSA-N-CNTs catalyst exhibits excellent stability in acidic

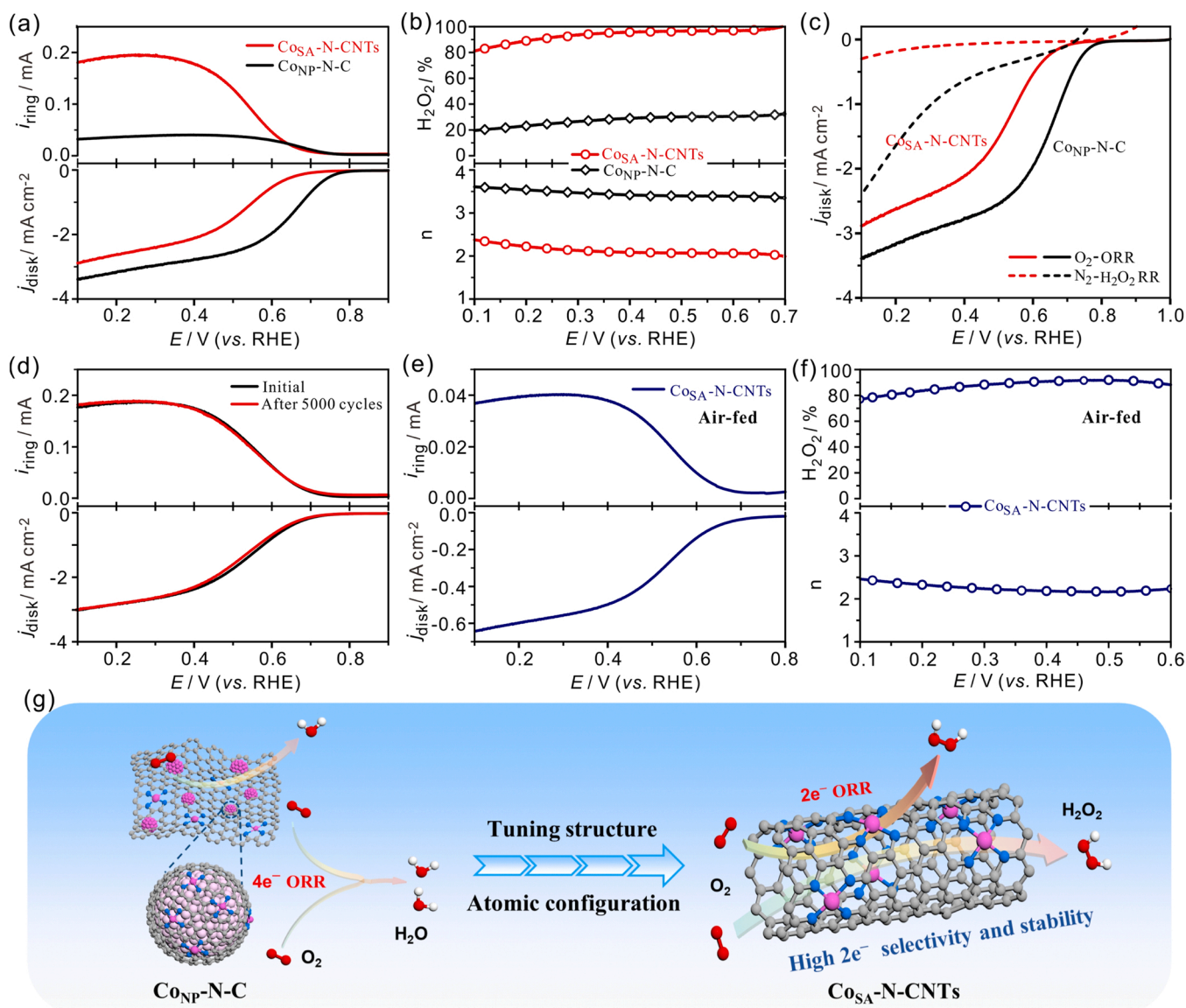


Fig. 4. Electrochemical ORR performance. (a) LSV curves and (b) corresponding calculated H₂O₂ selectivity (H₂O₂/%) and electron transfer number (n) at 1600 rpm with a scan rate of 10 mV s⁻¹ in an O₂-saturated 0.5 M H₂SO₄ electrolyte. (c) LSV curves for H₂O₂RR are recorded in N₂-saturated 0.5 M H₂SO₄ containing 10 mM H₂O₂. (d) Polarization curves of Co_{SA}-N-CNTs initially and after 5000 CV scanning cycles. (e) LSV curves and (f) corresponding calculated H₂O₂ selectivity (H₂O₂/%) and electron transfer number (n) of Co_{SA}-N-CNTs under air-fed conditions. (g) The schematic diagram for the main ORR pathways of Co_{NP}-N-C and Co_{SA}-N-CNTs.

media. As shown in Fig. 4d, after 5000 continuous cycles of accelerated durability test (ADT), Co_{SA}-N-CNTs catalyst shows scarcely attenuation in comparison with the initial curve, and the half-wave potential shifts negatively of 1 mV only. In addition, the stability of the Co_{SA}-N-CNTs catalyst is also analyzed by chronoamperometry using RRDE system (Fig. S6). After more than 10 h of testing, neither the disk nor the ring current attenuates significantly. The morphology and structural state change of Co_{SA}-N-CNTs after stability testing were performed by AC STEM and XPS, as displayed in Fig. S7. The AC STEM image reveals that the isolated Co atoms are highly dispersed on the carbon nanotubes. And the high-resolution Co 2p spectra of the catalyst before and after the stability testing are almost the same, further indicating the structural stability of the atomic Co-N_x species in Co_{SA}-N-CNTs. The above results indicate that the Co_{SA}-N-CNTs catalyst has excellent stability in an acidic environment and is suitable for the long-term electrochemical application. This is mainly due to the highly stable structure of Co_{SA}-N-CNTs catalysts, as the retained active Co-N_x species are strongly coordinated and embedded into the graphitized carbon nanotube after undergoing

intense high-temperature pyrolysis reduction and acid-leaching processes. More remarkably, under the air-fed condition, the as-fabricated Co_{SA}-N-CNTs catalyst also shows an excellent 2e⁻ ORR performance (Fig. 4e), in spite that the Co_{SA}-N-CNTs catalyst displays lower ring and disk current densities compared with it under the pure O₂ condition. The H₂O₂ selectivity can also reach ~90% in the potential range of 0.35–0.6 V (Fig. 4f), which means the great potential of the real application.

3.3. Comparison of catalysts at different temperatures

Further, to investigate the affecting factors of the oxygen reduction selectivity, the Co-N-CNTs-X (X = 700–1000 °C) samples were prepared under H₂ atmosphere at different temperatures were compared. As described from the SEM images of Figs. 5a–d and S8, all the obtained Co-N-CNTs-X samples present well-defined CNTs structures, whereas the contrast samples under argon atmosphere (Fig. S9) retain the initial morphology. This phenomenon is mainly that the reducing gas (H₂) will

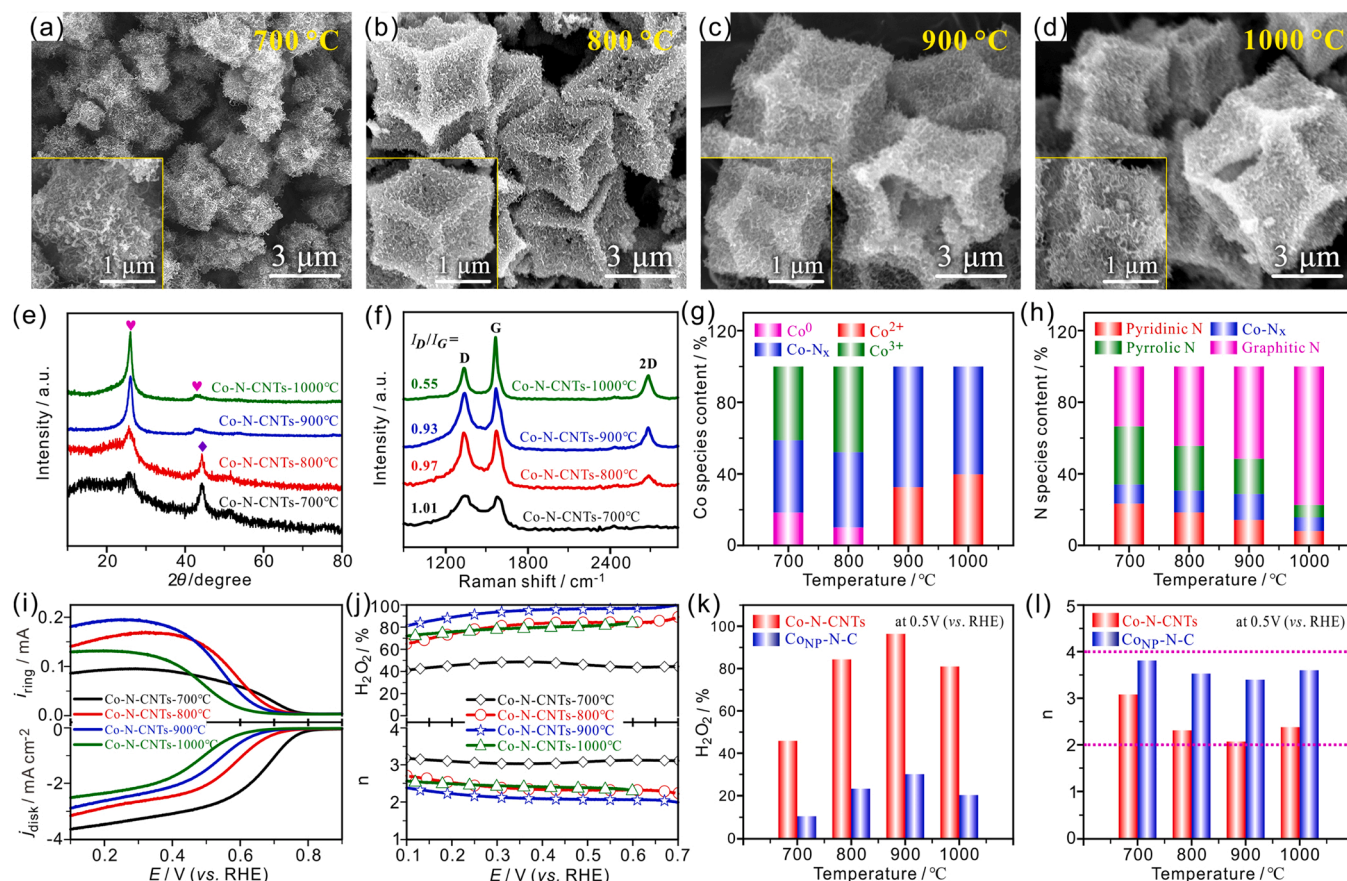


Fig. 5. (a-d) SEM images, (e) XRD patterns, (f) Raman spectra, (g) and (h) The cobalt and nitrogen species content results from XPS fitting data, (i) LSV curves, and (j) corresponding calculated H_2O_2 selectivity ($\text{H}_2\text{O}_2/\%$) and electron transfer number (n) of Co-N-CNTs-X samples. (k) Comparison of the H_2O_2 selectivity ($\text{H}_2\text{O}_2/\%$) and (l) electron transfer number (n) of Co-N-CNTs-X and CoNP-N-C-X at 0.5 V (vs. RHE) potential.

preferentially transform metal ions during the pyrolysis process into metal nano-catalysts, which then catalyze the remaining organic units to form CNTs [19,36]. With the increase of temperature, the diffraction peak of C (002) gradually becomes sharper, whereas the metallic Co peaks gradually weaken, and then disappear (Fig. 5e). The Co-N bonds will be greatly broken, leading to the migration and aggregation of the Co atoms to form large-sized nanoparticles at high temperature, as proved by XRD patterns in Fig. S10, which can be easily removed by acid-leaching. On the other hand, the hydrogen etching effect in the high temperatures (900 and 1000 °C) are more violent than that in the relatively low temperatures (700 and 800 °C). Thus, the Co-N-CNTs samples prepared at the high temperature will possess more voids and vacancies in the carbon matrix, making the acid solution is easier to enter the interior of the material, which can also promote the removal of cobalt nanoparticles during the acid-leaching process (Figs. S11 and S12) [37]. The Raman spectra of Fig. 5f show that the I_D/I_G values gradually decrease and the 2D peak intensity increases, which means that the degree of graphitization increases. The XPS results (Fig. S13 and Table S3) show that the Co contents gradually decrease, and no metallic Co is detected in the samples at 900 and 1000 °C (Fig. 5g). Fig. 5h shows that the proportion of graphitic-N gradually increases, which is conducive to improving the structure and electrochemical stability of the catalyst [38,39]. Most importantly, Co-N-CNTs-900 °C has the highest levels of Co-N_x species (Tables S4 and S5), and the higher temperature is not conducive to its retention.

Fig. 5i shows the polarization curves of Co-N-CNTs-X samples. In terms of onset potential and diffusion-limiting current density, the ORR activity gradually decreases with increasing temperature, which is mainly due to the loss of Co content, indicating that cobalt plays an

important role in the activity of $2e^-$ ORR. The calculated $\text{H}_2\text{O}_2/\%$ and n values (Fig. 5j) show that the Co-N-CNTs-900 °C catalyst has the best H_2O_2 selectivity, which is mainly attributed to the highest proportion of Co-N_x species, as well as high degree of graphitization property. In addition, according to the electrochemical performance of the CoNP-N-C-X (Fig. S14), the comparison of $\text{H}_2\text{O}_2/\%$ and n values (Figs. 5k and l) of Co-N-C catalysts with different structures and atomic configurations also show that Co-N-CNTs-X catalysts are more suitable for the H_2O_2 electrosynthesis than CoNP-N-C-X samples. The above results reveal that CoSA-N-CNTs catalyst has the integrated merits of the three-dimensional interconnected porous frameworks by carbon nanotube networks, exposing more strongly coordinated atomically dispersed Co-N_x active species are more favorable for improving the $2e^-$ ORR selectivity, whereas the presence of abundant Co nanoparticles is disadvantageous, which can also be corroborated in the previous literature [40,41]. Therefore, this can guide the rational design and regulation of electrocatalysts toward the target application.

To elucidate the distinction of electrocatalytic performance on the two different atomic configurations, density functional theory (DFT) calculations were performed. The possible slab models of Co-N₄ and CoNP-Co-N_4 systems were built employed for the DFT calculations, as shown in Figs. S16 and S17. The free energy diagrams (Fig. S18) show that the free energy value of the Co-N₄ structure is 3.38 eV, which is close to the optimal value (3.52 eV), implying that it is more conducive to the $2e^-$ reaction pathway. Based on the Sabatier theory, the activity of the $2e^-$ ORR is determined by the adsorption and desorption processes of $^*\text{OOH}$, thus the $^*\text{OOH}$ adsorption free energy ($\Delta G_{^*\text{OOH}}$) is usually used as a descriptor to elucidate its activity [42,43]. The 'volcanic relationship' curve plotted by $\Delta G_{^*\text{OOH}}$ (Fig. S19) demonstrates that the single

Co–N₄ active site has a good 2e[−] ORR activity, whereas Co_{NP}–Co–N₄ system shows a significant 4e[−] ORR tendency. Furthermore, the differential charge densities diagrams (Fig. S20) explain that the introduction of nanoparticles will change the charge distribution of the Co–N₄ moiety, in particular the surrounding nitrogen atoms which have almost no electrons distribution, leading to undesirable effects between *OOH intermediates and sites [44]. Besides, the bond length of O–O (1.43 Å) in Co–N₄ system is shorter than Co_{NP}–Co–N₄ system (1.45 Å) due to the electronic effect (Fig. S21), which means *HOO intermediates more difficult to cleave the O–O bond, resulting in more favorable H₂O₂ formation [45]. The above theoretical analysis shows that Co–N₄ active site has a good 2e[−] ORR tendency to generate H₂O₂, while the combination of Co nanoparticles will be further reduction of H₂O₂ product, leading to the 4e[−] process, which is in good consistent with the previous H₂O₂RR results.

3.4. H₂O₂ yield measurements and pollutant degradation

To verify the actual ability of the Co_{SA}-N-CNTs catalyst, the catalyst loaded on carbon fiber paper (CFP) was monitored to electrochemically synthesize H₂O₂ in real-time by chronoamperometry method using a self-assembled three-electrode flow cell (Fig. S22). Firstly, the pure CFP substrate was performed (Fig. S23), showing that there is almost no activity and H₂O₂ yield in an acidic media, so the interference of CFP can be eliminated. Subsequently, the H₂O₂ yield and Faraday efficiency (FE) (Fig. 6a) at different potentials are derived by chronoamperometry measurements (Fig. S24), displaying the maximum current and the optimal H₂O₂ production capacity at 0 V (vs. RHE) (Fig. S25). Therefore, we finally choose to carry out H₂O₂ yield accumulation test at 0 V. Figs. 6b and S26 show the accumulation of the H₂O₂ yield and the corresponding FEs. After 180 min of testing, the total accumulation yield of H₂O₂ is approximately 4700 mg L^{−1}. Where the yield of H₂O₂ and FE (86%~80%) will decrease slightly over time, due to the accumulation of H₂O₂ in the electrolyte leading to the increase of the peroxide reduction reaction rate. [28] The results show that the generation rate of H₂O₂ production can reach 974 ± 25 mmol g_{cat}^{−1} h^{−1},

which is much higher than the previously reported results in the acidic environment (Fig. 6c and Table S7). Notably, when employed in the air condition, as shown in Figs. 6d and S27, the electrode assembled by Co_{SA}-N-CNTs catalyst also achieves a high H₂O₂ accumulation yield with 900 mg L^{−1} after 180 min at 0 V, indicative of the great potential of practical application. Thus, to demonstrate the practicability of our designed Co_{SA}-N-CNTs catalyst, the electrochemical degradation of organic substances based on malachite green and methyl blue with the concentration of 50 mg L^{−1} was performed. As exhibited in Fig. 6e and f show the fast degradation performance with just a few or tens of minutes, indicative of the superb practicability. The above results reveal that the Co_{SA}-N-CNTs catalyst not only shows excellent H₂O₂ production ability but also exhibits a high degradation efficiency to organic pollutants.

4. Conclusion

In summary, Co-N-C materials with different structures were successfully synthesized by the pyrolysis of the metal-organic frameworks precursors. The as-prepared Co_{NP}-N-C with dominated Co nanoparticles shows obvious 4e[−] ORR performance. Inversely, the constructed Co_{SA}-N-CNTs catalyst with atomically dispersed cobalt atoms possesses superb 2e[−] selectivity and stability towards ORR. This tunability is ascribed to the modification of the structure and cobalt atomic configuration properties. When equipped with the Co_{SA}-N-CNTs catalyst in a flow cell, it exhibits superhigh H₂O₂ production and enables efficiently degrading organics pollutants, indicative of an idea catalyst for H₂O₂ electrosynthesis. The results revealed that the Co_{SA}-N-CNTs with three-dimensional conductive carbon nanotubes framework structure can effectively expose more atomically dispersed Co–N_x species identified as the ORR active site and selective origin of 2e[−] pathway, whereas abundant Co nanoparticles are more favorable for the 4e[−] ORR. This work provides insight into the controllable fabrication of highly active and stable catalysts to tune the ORR selectivity for various products and applications in acidic environments.

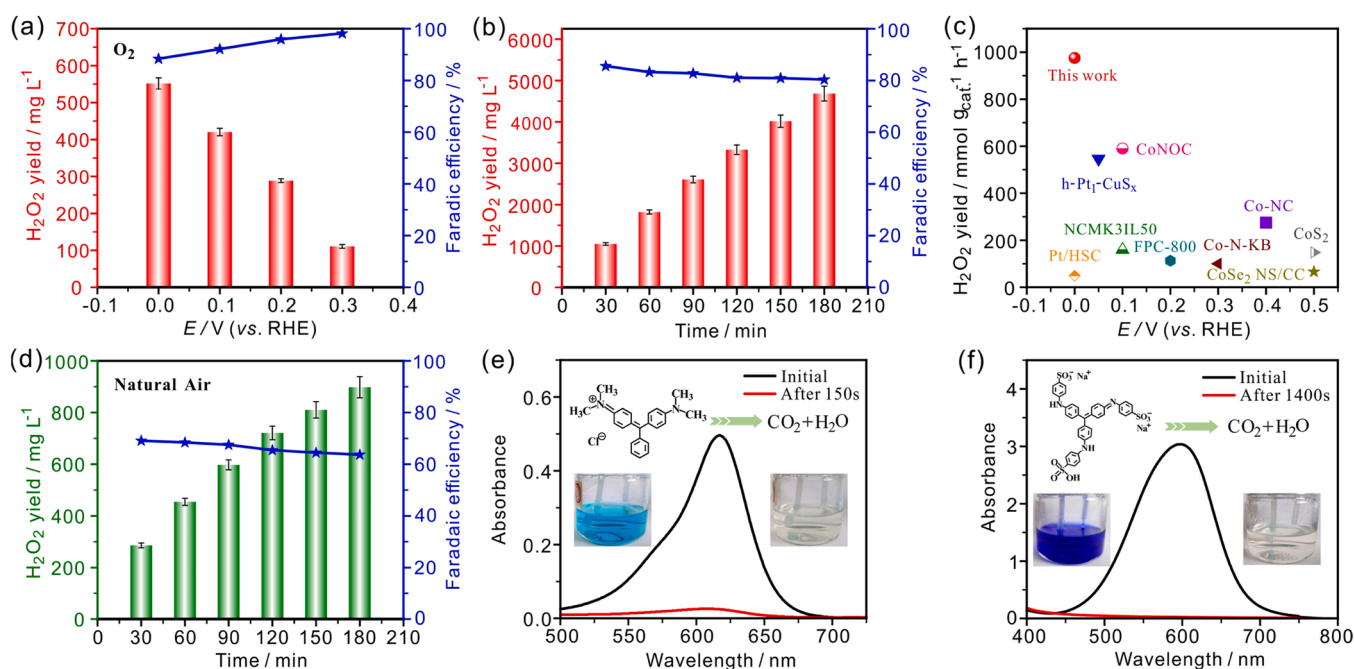


Fig. 6. (a) The yield of H₂O₂ and Faraday efficiency at different potentials and (b) the accumulation of H₂O₂ yield and Faraday efficiency for electrolyzing 180 min at 0 V (vs. RHE) based on Co_{SA}-N-CNTs electrode. (c) Comparisons of the H₂O₂ yield of Co_{SA}-N-CNTs and other recently reported catalysts in acidic media. (d) The yield of H₂O₂ and Faraday efficiency after electrolysis for 180 min at 0 V (vs. RHE) under natural air conditions. Comparison of absorbance curves and optical images before and after degradation of (e) malachite green and (f) methyl blue (50 mg L^{−1}) at a current of ~30 mA by three-electrode flow cells, respectively.

CRediT authorship contribution statement

Wei Liu: Conceptualization, Methodology, Investigation, Formal analysis, Data curation, Writing – original draft. **Chang Zhang:** Investigation, Data curation, Visualization. **Jingjing Zhang:** Investigation, Formal analysis, Validation. **Xiao Huang:** Investigation, Validation. **Min Song:** Investigation, Validation. **Jingwen Li:** Investigation, Visualization. **Feng He:** Investigation, Visualization. **Jian Zhang:** Supervision, Writing – review & editing, Project administration, Funding acquisition. **Deli Wang:** Supervision, Writing – review & editing, Project administration, Funding acquisition.

Declaration of Competing Interest

The authors declare that they have no known competing financial interests or personal relationships that could have appeared to influence the work reported in this paper.

Acknowledgements

This work was supported by the National Natural Science Foundation of China (91963109), the Foundation of State Key Laboratory of Coal Combustion (FSKLCCA2008), and the Key Laboratory of Hubei Province for Coal Conversion and New Carbon Materials (Wuhan University of Science and Technology) (WKDM202101). The authors thank the support of the Analytical and Testing Center of Huazhong University of Science & Technology for SEM, XPS and Raman measurements.

Appendix A. Supporting information

Supplementary data associated with this article can be found in the online version at doi:10.1016/j.apcatb.2022.121312.

References

- [1] J. Zhang, H. Yang, B. Liu, Coordination engineering of single-atom catalysts for the oxygen reduction reaction: a review, *Adv. Energy Mater.* 11 (2021), 2002473, <https://doi.org/10.1002/aenm.202002473>.
- [2] W. Zhu, Y. Pei, J.C. Douglas, J. Zhang, H. Zhao, J. Xue, Q. Wang, R. Li, Y. Qin, Y. Yin, D.R. Dekel, M.D. Guiver, Multi-scale study on bifunctional Co/Fe–N–C cathode catalyst layers with high active site density for the oxygen reduction reaction, *Appl. Catal. B Environ.* 299 (2021), 120656, <https://doi.org/10.1016/j.apcatb.2021.120656>.
- [3] T.H. Jeon, B. Kim, C. Kim, C. Xia, H. Wang, P.J.J. Alvarez, W. Choi, Solar photoelectrochemical synthesis of electrolyte-free H₂O₂ aqueous solution without needing electrical bias and H₂, *Energy Environ. Sci.* 14 (2021) 3110–3119, <https://doi.org/10.1039/D0EE03567J>.
- [4] C. Zhang, J. Zhang, J.J. Zhang, M. Song, X. Huang, W. Liu, M. Xiong, Y.Q. Chen, S. W. Xia, H.P. Yang, D.L. Wang, Tuning coal into graphene-like nanocarbon for electrochemical H₂O₂ production with nearly 100% faraday efficiency, *ACS Sustain. Chem. Eng.* 9 (2021) 9369–9375, <https://doi.org/10.1021/acssuschemeng.1c02357>.
- [5] S. Anantharaj, S. Pitchaimuthu, S. Noda, A review on recent developments in electrochemical hydrogen peroxide synthesis with a critical assessment of perspectives and strategies, *Adv. Colloid Interface Sci.* 287 (2021), 102331, <https://doi.org/10.1016/j.cis.2020.102331>.
- [6] Y. Wu, Z. Gao, Y. Feng, Q. Cui, C. Du, C. Yu, L. Liang, W. Zhao, J. Feng, J. Sun, R. Yang, J. Sun, Harnessing selective and durable electrosynthesis of H₂O₂ over dual-defective yolk-shell carbon nanosphere toward on-site pollutant degradation, *Appl. Catal. B Environ.* 298 (2021), 120572, <https://doi.org/10.1016/j.apcatb.2021.120572>.
- [7] K. Jiang, J. Zhao, H. Wang, Catalyst design for electrochemical oxygen reduction toward hydrogen peroxide, *Adv. Funct. Mater.* 30 (2020), 2003321, <https://doi.org/10.1002/adfm.202003321>.
- [8] Y. Wang, D. Wang, Y. Li, A fundamental comprehension and recent progress in advanced Pt-based ORR nanocatalysts, *SmartMat* 2 (2021) 56–75, <https://doi.org/10.1002/smm2.1023>.
- [9] Y. Wang, G.L.N. Waterhouse, L. Shang, T. Zhang, Electrocatalytic oxygen reduction to hydrogen peroxide: from homogeneous to heterogeneous electrocatalysis, *Adv. Energy Mater.* 11 (2021), 2003323, <https://doi.org/10.1002/aenm.202003323>.
- [10] S. Siahrostami, A. Verdaguier-Casadevall, M. Karamad, D. Deiana, P. Malacrida, B. Wickman, M. Escudero-Escribano, E.A. Paoli, R. Frydendal, T.W. Hansen, I. Chorkendorff, I.E.L. Stephens, J. Rossmeisl, Enabling direct H₂O₂ production through rational electrocatalyst design, *Nat. Mater.* 12 (2013) 1137–1143, <https://doi.org/10.1038/nmat3795>.
- [11] J.S. Jirkovsky, I. Panas, E. Ahlberg, M. Halasa, S. Romani, D.J. Schiffrin, Single atom hot-spots at Au-Pd nanoalloys for electrocatalytic H₂O₂ production, *J. Am. Chem. Soc.* 133 (2011) 19432–19441, <https://doi.org/10.1021/ja206477z>.
- [12] A. Verdaguier-Casadevall, D. Deiana, M. Karamad, S. Siahrostami, P. Malacrida, T. W. Hansen, J. Rossmeisl, I. Chorkendorff, I.E.L. Stephens, Trends in the electrochemical synthesis of H₂O₂: enhancing activity and selectivity by electrocatalytic site engineering, *Nano Lett.* 14 (2014) 1603–1608, <https://doi.org/10.1021/nl500037x>.
- [13] Y. Jia, X. Yao, Atom-coordinated structure triggers selective H₂O₂ production, *Chem* 6 (2020) 548–550, <https://doi.org/10.1016/j.chempr.2020.02.011>.
- [14] J. Gao, H. Yang, X. Huang, S.-F. Hung, W. Cai, C. Jia, S. Miao, H.M. Chen, X. Yang, Y. Huang, T. Zhang, B. Liu, Enabling direct H₂O₂ production in acidic media through rational design of transition metal single atom catalyst, *Chem* 6 (2020) 658–674, <https://doi.org/10.1016/j.chempr.2019.12.008>.
- [15] S. Li, Y. Gao, N. Li, L. Ge, X. Bu, P. Feng, Transition metal-based bimetallic MOFs and MOF-derived catalysts for electrochemical oxygen evolution reaction, *Energy Environ. Sci.* 14 (2021) 1897–1927, <https://doi.org/10.1039/D0EE03697H>.
- [16] Y. Tan, Z. Zhang, Z. Lei, L. Yu, W. Wu, Z. Wang, N. Cheng, Electronic modulation optimizes OH* intermediate adsorption on Co–N_x–C sites via coupling CoNi alloy in hollow carbon nanopolyhedron toward efficient reversible oxygen electrocatalysis, *Appl. Catal. B Environ.* (2021), 121006, <https://doi.org/10.1016/j.apcatb.2021.121006>.
- [17] M.X. Chen, M.Z. Zhu, M. Zuo, S.Q. Chu, J. Zhang, Y. Wu, H.W. Liang, X.L. Feng, Identification of catalytic sites for oxygen reduction in metal/nitrogen-doped carbons with encapsulated metal nanoparticles, *Angew. Chem. Int. Ed.* 59 (2020) 1627–1633, <https://doi.org/10.1002/ange.201912275>.
- [18] Q.Q. Cheng, S.B. Han, K. Mao, C. Chen, L.J. Yang, Z.Q. Zou, M. Gu, Z. Hu, H. Yang, Co nanoparticle embedded in atomically-dispersed Co–N–C nanofibers for oxygen reduction with high activity and remarkable durability, *Nano Energy* 52 (2018) 485–493, <https://doi.org/10.1016/j.nanoen.2018.08.005>.
- [19] B.Y. Xia, Y. Yan, N. Li, H.B. Wu, X.W. Lou, X. Wang, A metal-organic framework-derived bifunctional oxygen electrocatalyst, *Nat. Energy* 1 (2016) 1–8, <https://doi.org/10.1038/nenergy.2015.6>.
- [20] W.B. Gong, Q.L. Yuan, C. Chen, Y. Lv, Y. Lin, C.H. Liang, G.Z. Wang, H.M. Zhang, H.J. Zhao, Liberating N–CNTs confined highly dispersed Co–N_x sites for selective hydrogenation of quinolines, *Adv. Mater.* 31 (2019), 1906051, <https://doi.org/10.1002/adma.201906051>.
- [21] Y. Zhu, W. Sun, J. Luo, W. Chen, T. Cao, L. Zheng, J. Dong, J. Zhang, M. Zhang, Y. Han, C. Chen, Q. Peng, D. Wang, Y. Li, A cocoon silk chemistry strategy to ultrathin N-doped carbon nanosheet with metal single-site catalysts, *Nat. Commun.* 9 (2018) 3861, <https://doi.org/10.1038/s41467-018-06296-w>.
- [22] W. Zhang, X.F. Jiang, X.B. Wang, Y.V. Kaneti, Y.X. Chen, J. Liu, J.S. Jiang, Y. Yamauchi, M. Hu, Spontaneous weaving of graphitic carbon networks synthesized by pyrolysis of ZIF-67 crystals, *Angew. Chem. Int. Ed.* 56 (2017) 8435–8440, <https://doi.org/10.1002/anie.201701252>.
- [23] Y.Y. Xu, P.L. Deng, G.D. Chen, J.X. Chen, Y. Yan, K. Qi, H.F. Liu, B.Y. Xia, 2D nitrogen-doped carbon nanotubes/graphene hybrid as bifunctional oxygen electrocatalyst for long-life rechargeable Zn–Air batteries, *Adv. Funct. Mater.* 30 (2020), 1906081, <https://doi.org/10.1002/adfm.201906081>.
- [24] Y. Pan, R. Lin, Y.J. Chen, S.J. Liu, W. Zhu, X. Cao, W.X. Chen, K.L. Wu, W. C. Cheong, Y. Wang, L.R. Zheng, J. Luo, Y. Lin, Y.Q. Liu, C.G. Liu, J. Li, Q. Lu, X. Chen, D.S. Wang, Q. Peng, C. Chen, Y.D. Li, Design of single-atom Co–N_x catalytic site: a robust electrocatalyst for CO₂ reduction with nearly 100% CO selectivity and remarkable stability, *J. Am. Chem. Soc.* 140 (2018) 4218–4221, <https://doi.org/10.1021/jacs.8b00814>.
- [25] S.M. Chen, L.T. Ma, S.L. Wu, S.Y. Wang, Z.B. Li, A.A. Emmanuel, M.R. Huq, C. Y. Zhi, J.A. Zapien, Uniform virus-like Co–N–Cs electrocatalyst derived from prussian blue analog for stretchable fiber-shaped Zn–Air batteries, *Adv. Funct. Mater.* 30 (2020), 1908945, <https://doi.org/10.1002/adfm.201908945>.
- [26] T. Liu, J. Mou, Z. Wu, C. Lv, J. Huang, M. Liu, A facile and scalable strategy for fabrication of superior bifunctional freestanding air electrodes for flexible zinc–air batteries, *Adv. Funct. Mater.* 30 (2020), 2003407, <https://doi.org/10.1002/adfm.202003407>.
- [27] X. Li, A.E. Surkus, J. Rabeah, M. Anwar, S. Dastagir, H. Junge, A. Bruckner, M. Beller, Cobalt single-atom catalysts with high stability for selective dehydrogenation of formic acid, *Angew. Chem. Int. Ed.* 59 (2020) 15849–15854, <https://doi.org/10.1002/anie.202004125>.
- [28] Y.Y. Sun, L. Silvioli, N.R. Sahaie, W. Ju, J.K. Li, A. Zitolo, S. Li, A. Bagger, L. Arnarson, X.L. Wang, T. Moeller, D. Bernsmeier, J. Rossmeisl, F. Jaouen, P. Strasser, Activity-selectivity trends in the electrochemical production of hydrogen peroxide over single-site metal–nitrogen–carbon catalysts, *J. Am. Chem. Soc.* 141 (2019) 12372–12381, <https://doi.org/10.1021/jacs.9b05576>.
- [29] Z.H. Li, M.F. Shao, L. Zhou, R.K. Zhang, C. Zhang, M. Wei, D.G. Evans, X. Duan, Directed growth of metal-organic frameworks and their derived carbon-based network for efficient electrocatalytic oxygen reduction, *Adv. Mater.* 28 (2016) 2337–2344, <https://doi.org/10.1002/adma.201505086>.
- [30] K. Fu, Y. Wang, L.C. Mao, X.X. Yang, J.H. Jin, S.L. Yang, G. Li, Strongly coupled Co, N co-doped carbon nanotubes/graphene-like carbon nanosheets as efficient oxygen reduction electrocatalysts for primary Zinc–air battery, *Chem. Eng. J.* 351 (2018) 94–102, <https://doi.org/10.1016/j.cej.2018.06.059>.
- [31] Y.J. Chen, R. Gao, S.F. Ji, H.J. Li, K. Tang, P. Jiang, H.B. Hu, Z.D. Zhang, H.G. Hao, Q.Y. Qu, X. Liang, W.X. Chen, J.C. Dong, D.S. Wang, Y.D. Li, Atomic-level modulation of electronic density at cobalt single-atom sites derived from metal-organic frameworks: enhanced oxygen reduction performance, *Angew. Chem. Int. Ed.* 60 (2021) 3212–3221, <https://doi.org/10.1002/anie.202012798>.

- [32] L.T. Yan, Y.L. Xu, P. Chen, S. Zhang, H.M. Jiang, L.Z. Yang, Y. Wang, L. Zhang, J. X. Shen, X.B. Zhao, L.Z. Wang, A freestanding 3D heterostructure film stitched by MOF-derived carbon nanotube microsphere superstructure and reduced graphene oxide sheets: a superior multifunctional electrode for overall water splitting and Zn-Air batteries, *Adv. Mater.* 32 (2020), 2003313, <https://doi.org/10.1002/adma.202003313>.
- [33] H.L. Fei, J.C. Dong, Y.X. Feng, C.S. Allen, C.Z. Wan, B. Voloskiy, M.F. Li, Z. P. Zhao, Y.L. Wang, H.T. Sun, P.F. An, W.X. Chen, Z.Y. Guo, C. Lee, D.L. Chen, I. Shakir, M.J. Liu, T.D. Hu, Y.D. Li, A.I. Kirkland, X.F. Duan, Y. Huang, General synthesis and definitive structural identification of MN_4C_4 single-atom catalysts with tunable electrocatalytic activities, *Nat. Catal.* 1 (2018) 63–72, <https://doi.org/10.1038/s41929-017-0008-y>.
- [34] H.L. Fei, J.C. Dong, C.Z. Wan, Z.P. Zhao, X. Xu, Z.Y. Lin, Y.L. Wang, H.T. Liu, K. T. Zang, J. Luo, S.L. Zhao, W. Hu, W.S. Yan, I. Shakir, Y. Huang, X.F. Duan, Microwave-assisted rapid synthesis of graphene-supported single atomic metals, *Adv. Mater.* 30 (2018), 1802146, <https://doi.org/10.1002/adma.201802146>.
- [35] C. Tang, L. Chen, H.J. Li, L.Q. Li, Y. Jiao, Y. Zheng, H.L. Xu, K. Davey, S.Z. Qiao, Tailoring acidic oxygen reduction selectivity on single-atom catalysts via modification of first and second coordination spheres, *J. Am. Chem. Soc.* 143 (2021) 7819–7827, <https://doi.org/10.1021/jacs.1c03135>.
- [36] J.S. Meng, C.J. Niu, L.H. Xu, J.T. Li, X. Liu, X.P. Wang, Y.Z. Wu, X.M. Xu, W. Y. Chen, Q. Li, Z.Z. Zhu, D.Y. Zhao, L.Q. Mai, General oriented formation of carbon nanotubes from metal-organic frameworks, *J. Am. Chem. Soc.* 139 (2017) 8212–8221, <https://doi.org/10.1021/jacs.7b01942>.
- [37] X.Q. Wang, Z. Chen, X.Y. Zhao, T. Yao, W.X. Chen, R. You, C.M. Zhao, G. Wu, J. Wang, W.X. Huang, J.L. Yang, X. Hong, S.Q. Wei, Y. Wu, Y.D. Li, Regulation of coordination number over single Co sites: triggering the efficient electroreduction of CO_2 , *Angew. Chem. Int. Ed.* 57 (2018) 1944–1948, <https://doi.org/10.1002/ange.201712451>.
- [38] M. Wu, G. Zhang, N. Chen, Y. Hu, T. Regier, D. Rawach, S. Sun, Self-reconstruction of Co/ Co_2P heterojunctions confined in N-doped carbon nanotubes for Zinc-Air flow batteries, *ACS Energy Lett.* 6 (2021) 1153–1161, <https://doi.org/10.1021/acseenergylett.1c00037>.
- [39] X. Liu, L. Wu, T. Liu, L. Zhang, In situ confine of $\text{Co}_3\text{ZnC}/\text{Co}$ in N-doped carbon nanotube-grafted graphitic carbon nanoflakes as 1D–2D hierarchical catalysts toward superior redox activity, *Appl. Catal. B Environ.* 281 (2021), 119513, <https://doi.org/10.1016/j.apcatb.2020.119513>.
- [40] X. Cheng, J. Yang, W. Yan, Y. Han, X. Qu, S. Yin, C. Chen, R. Ji, Y. Li, G. Li, L. Y. Jiang, S. Sun, Nano-geometric deformation and synergistic Co nanoparticles–Co– N_4 composite sites for proton exchange membrane fuel cells, *Energy Environ. Sci.* 14 (2021) 5958–5967, <https://doi.org/10.1039/D1EE01715B>.
- [41] E. Jung, H. Shin, B.-H. Lee, V. Efremov, S. Lee, H.S. Lee, J. Kim, W. Hooch Antink, S. Park, K.-S. Lee, S.-P. Cho, J.S. Yoo, Y.-E. Sung, T. Hyeon, Atomic-level tuning of Co–N–C catalyst for high-performance electrochemical H_2O_2 production, *Nat. Mater.* 19 (2020) 436–442, <https://doi.org/10.1038/s41563-019-0571-5>.
- [42] Z. Lu, G. Chen, S. Siahrostami, Z. Chen, K. Liu, J. Xie, L. Liao, T. Wu, D. Lin, Y. Liu, T.F. Jaramillo, J.K. Nørskov, Y. Cui, High-efficiency oxygen reduction to hydrogen peroxide catalysed by oxidized carbon materials, *Nat. Catal.* 1 (2018) 156–162, <https://doi.org/10.1038/s41929-017-0017-x>.
- [43] H.N. Fernandez-Escamilla, J. Guerrero-Sanchez, E. Contreras, J.M. Ruiz-Marizcal, G. Alonso-Nunez, O.E. Contreras, R.M. Felix-Navarro, J.M. Romo-Herrera, N. Takeuchi, Understanding the selectivity of the oxygen reduction reaction at the atomistic level on nitrogen-doped graphitic carbon materials, *Adv. Energy Mater.* 11 (2021), 2002459, <https://doi.org/10.1002/aenm.202002459>.
- [44] X.H. Zhao, Y.Y. Liu, Origin of selective production of hydrogen peroxide by electrochemical oxygen reduction, *J. Am. Chem. Soc.* 143 (2021) 9423–9428, <https://doi.org/10.1021/jacs.1c02186>.
- [45] Q.R. Zhang, X. Tan, N.M. Bedford, Z.J. Han, L. Thomsen, S. Smith, R. Amal, X. Y. Lu, Direct insights into the role of epoxy groups on cobalt sites for acidic H_2O_2 production, *Nat. Commun.* 11 (2020) 1–11, <https://doi.org/10.1038/s41467-020-17782-5>.